Research Square

Preprints are preliminary reports that have not undergone peer review.
They should not be considered conclusive, used to inform clinical practice,
or referenced by the media as validated information.

Surface Directed Flows and Fluidic diodes: Transforming lateral flow assays into multistep diagnostics devices

Selina Cervantes
Northern Illinois University
Haydon Hill
University of Nevada
Jacob Dayton
University of Nevada
David AuCoin
University of Nevada
Venumadhav Korampally
vkorampally@niu.edu

Northern Illinois University

Research Article

Keywords:

Posted Date: November 4th, 2026

DOI: https://doi.org/10.21203/rs.3.rs-11067801/v1

License: This work is licensed under a Creative Commons Attribution 4.0 International License.
Read Full License

Additional Declarations: No competing interests reported.

Surface Directed Flows and Fluidic diodes: Transforming lateral flow assays into multistep diagnostics devices

Selina Cervantes[a], Haydon Hill[b], Jacob Dayton[b], David AuCoin[b], Venumadhav Korampally[a,*]

[a] Department of Electrical Engineering, Northern Illinois University, DeKalb, Illinois, USA

[b] Department of Microbiology and Immunology, University of Nevada, Reno, Nevada, USA

*** Corresponding Author:** Venumadhav Korampally, Professor, Department of Electrical Engineering, Northern Illinois University, DeKalb, Illinois, USA. E-mail: vkorampally@niu.edu

Abstract: Lateral flow assays (LFAs) are among the most widely deployed point-of-care diagnostic platforms, yet their inherent single-flow architecture limits their operation to single-step binding assays and precludes the sequential delivery of multiple reagents within a single device. Herein, we report the design, fabrication, and characterization of hybrid paper-plastic fluidic diode modules that may be seamlessly integrated into conventional LFA architectures to enable controlled, unidirectional, multi-step reagent delivery. Single diode characterization confirmed reliable forward flow initiation and robust reverse flow prevention across a range of buffer compositions with results in good agreement with the theoretical predictions. Cascaded diode assemblies demonstrated well-defined sequential reagent delivery with minimal inter-zone mixing. Integration of a two-stage cascaded diode assembly into a SARS-CoV-2 lateral flow assay demonstrated a 2.5-fold enhancement in test line signal intensity relative to a conventional single-flow LFA employing identical assay chemistries. Owing to the simple geometry of the fluidic diode, these components may be assembled as a planar laminated stack along with other LFA components and singulated into individual test strips through the same cutting operations

employed in conventional LFA manufacturing, without any requirement for precision microfabrication or specialized equipment. This positions the fluidic diode as a manufacturable and scalable solution for introducing multi-step reagent sequencing into lateral flow diagnostics.

1. Introduction:

Lateral flow assays (LFAs) are among the most widely deployed point-of-care diagnostic platforms, owing to their low cost, ease of use, and reliable diagnostic performance under resource-limited settings. The underlying operational principle of these devices relies on the passive, capillary-driven transport of fluid through a series of overlapping porous membranes, without the requirement for external pumps or instrumentation[1], [2]. It is this simplicity of design that has been central to their widespread adoption, particularly in decentralized healthcare settings. However, this same design simplicity imposes fundamental constraints on fluid control within these devices. From a fluid transport standpoint, LFAs operate on passive fluid transport wherein fluid motion is governed almost entirely by the intrinsic wicking properties of the overlapped porous materials employed. While this works well for simple, single step binding assays, it leaves little opportunity to introduce and sequentially deliver multiple reagents through the device in a controlled manner. As a result, many of the advanced capabilities of lab-on-chip based microfluidic devices, including sequential reagent delivery[3], [3], [4], [5], autonomous flow gating[6], [7], [8], and multi-step reaction workflows, remain largely inaccessible within standard LFA formats, limiting conventional LFAs to single-step binding assays.

The advantages of multi-step workflows in lateral flow diagnostics are well established. Secondary amplification reactions performed subsequent to initial test-line formation have been shown to markedly enhance assay sensitivity[9], [10], [11]. For LFAs relying on electrochemical reactions for signal generation, a separate substrate introduction step following the enzyme linked detection antibody bonding at the test line is often necessitated[12], [13], [14]. In most reported literature, these additional reagents are introduced manually either through the same sample application

port or through direct application over the test line via the nitrocellulose viewing window. While such procedures are feasible when performed by trained users under controlled laboratory conditions, they are poorly suited to the user-friendly, decentralized point-of-care context in which LFAs find their greatest utility.

Recent efforts to introduce programmable flow control into paper-based assays have demonstrated increasingly complex assay workflows, including sequential autonomous reagent delivery and multi-step signal amplification. Approaches such as the use of thermally actuated wax valves[15], [16], passive flow timers[17], [18], and externally actuated microfluidic gates[19], [20], [21], [22], [23] have shown considerable promise in regulating flow behavior within paper-based devices. It should be noted, however, that many of these strategies introduce significant fabrication complexity, depend on external actuation mechanisms, or are incompatible with existing LFA manufacturing and testing paradigms, thereby limiting their ability to scale for wider adoption.

To that end, we introduce herein hybrid paper–plastic fluidic diode modules that may be seamlessly incorporated into conventional LFA architectures to enable controlled, sequential delivery of multiple reagents within a single device. The fluidic diode enforces unidirectional capillary-driven flow from a designated source pad to a downstream drain pad, while preventing reverse transport. When multiple such diodes are cascaded and interfaced with a conventional LFA strip, the enforced directionality of each stage facilitates multi-step sequenced reagent delivery to the LFA test zone thereby transforming conventional LFA strips to be compatible with multi-step binding assays.

To demonstrate the practical utility of this approach, we have integrated the cascaded fluidic diode architecture to produce a two-step binding SARS-CoV-2 Lateral flow assay (Here from referred to as the two stage LFA). These devices are constructed to decouple the sample and conjugate flows such that the sample is delivered first to the test line, followed by the conjugate. Device

performance was evaluated by directly comparing flow behavior and detection outcomes against a conventional single-flow LFA employing identical assay chemistries and testing conditions. These results demonstrate that the fluidic diode is a versatile and manufacturable modular component for introducing multi-step reagent sequencing into lateral flow diagnostics, while preserving the materials simplicity, fabrication compatibility, and user-friendliness that are central to the platform's broad appeal.

Results and Discussion:

2. Design and Operating Principles of the Fluidic Diode

2.1 Device Architecture

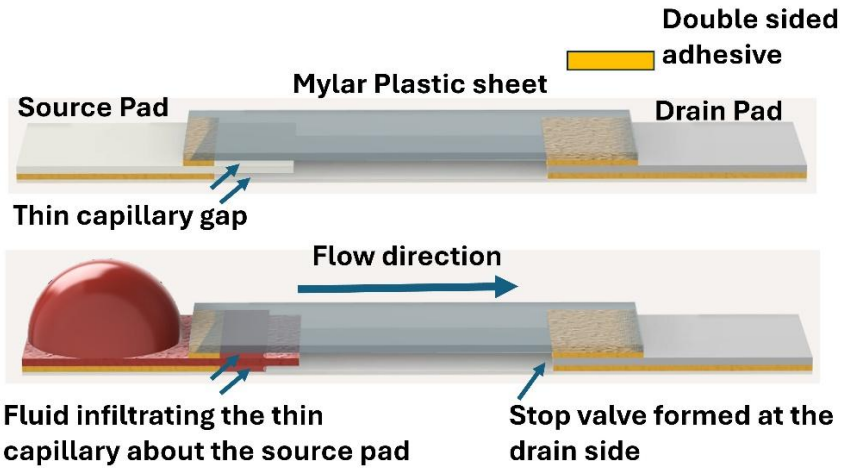


Figure 1: Schematic of an isolated fluidic diode illustrating the seamless forward flow mechanism

Figure 1 shows the schematic of an isolated fluidic diode. The device is constructed to contain two discrete paper pads, a source pad and a drain pad with a deliberate offset between them and affixed to the backing sheet. These pads are bridged with a hydrophilic mylar plastic sheet thereby creating an airgap between the pads. It is the asymmetry in the manner of bridging by the bottom backing sheet and the top mylar sheet that is central to the diode-like behavior of the device. On the source side, a hydrophobic double sided adhesive tape (DST) fixes the source pad to the top mylar sheet and the bottom backing card introducing a thin capillary gap on the top and the bottom of the paper pad. The thickness of this gap is defined by the DST thickness and is typically on the order of a few tens of micrometers. On the drain side, DST sandwiches the drain pad on both its top and bottom surfaces remaining flush with the drain pad face. It is this sandwiching configuration, in combination with the hydrophobicity of the DST surfaces and the abrupt geometric transition at the air-gap entrance, that gives rise to an effective capillary stop valve at the drain end of the device. Together, these two geometrically distinct DST configurations produce the unidirectional flow behavior characteristic of the fluidic diode, as described in the following sections.

2.2 Forward Flow behavior

When sample/buffer solution is applied to the source pad, the paper pad first becomes saturated through capillary imbibition. Once saturated, excess liquid begins to wick into the narrow capillary air gap formed above and below the source pad. Capillary pressure acts to draw the liquid forward along the top mylar and the bottom backing card, transitioning into the airgap separating the source and the drain pad. It should be noted that unlike enclosed microfluidic channels, this air gap here is open along its lateral sides; fluid confinement within the airgap is not provided by physical walls but rather fluid flow through the airgap occurs through surface-directed flow[24].

At this point, the capillary driving pressure acting on the fluid front may be calculated by considering fluid flow between two parallel hydrophilic surfaces of gap height h and is given by:

$$\Delta P_{forward} = \frac{2\gamma \cos\theta_v}{h} + \rho g H$$

where γ is the surface tension of the liquid and θ_v is the advancing contact angle of the liquid on the Mylar surface, ρ is the liquid density, g is the gravitational acceleration, and H is the effective hydrostatic head (the height of the liquid over the source pad). Having Mylar surfaces that are hydrophilic ($\theta_v < 90°$), this driving pressure is positive and acts to rapidly draw the fluid across the remainder of the air gap and into the drain pad. The impedance to flow in the forward direction is therefore minimal.

2.3 Reverse Flow Prevention

When fluid is applied to the drain pad and attempts to flow in the reverse direction, i.e from drain toward source, it encounters a fundamentally different geomety at the air-gap entrance. As described in Section 2.1 (fig. 1), DST sandwiches the drain pad on both its top and bottom surfaces remaining flush with its face within the gap. Consequently, the fluid exiting the drain pad at the air-gap entrance is simultaneously confronted by hydrophobic DST surfaces on both its top and bottom faces, together with an abrupt increase in the effective gap height at the transition from the paper pad thickness to the open air gap. The effective creation of a stop valve pins the advancing meniscus at the DST edges and the fluid fails to advance into the airgap (reverse flow). For the stop valve to burst, the meniscus must bulge until the contact angle with the DST surface reaches the critical advancing contact angle θ_A[25].

For the open two-surface geometry of the air gap, the maximum burst pressure may be estimated from the Young–Laplace equation applied to a fluid meniscus spanning two parallel surfaces of separation h - the thickness of the paper pad that is being sandwiched between the top and bottom DSTs:

$$\Delta P_{burst} = \frac{2\gamma \cos \theta_I^*}{h}$$

where $\theta_I^* = \min\{\theta_A + \beta, 180°\}$ is the maximum contact angle attained at the pinning edge, β is the divergence angle of the geometric transition at the DST–air gap interface, and h is the paper pad thickness[25]. It is reasonable to expect that for the geometry realized here, the combined hydrophobicity of the DST surface ($\theta_A > 90°$) and the near-orthogonal step transition ($\beta \approx 90°$) readily satisfies the condition $\theta_A + \beta \geq 180°$, such that $\theta_I^* = 180°$ and the burst pressure simplifies to:

$$\Delta P_{burst} = -\frac{2\gamma}{h}$$

It should be further noted that the sign of ΔP_{burst} is now negative, the hydrophobic DST surfaces and the geometric step transition together generate a resisting capillary pressure that actively opposes the reverse advancing meniscus, in contrast to the positive capillary driving pressure that facilitates forward flow across the hydrophilic Mylar surfaces. For a paper pad thickness of 0.28 mm and the surface tension of aqueous buffer (72mN/m), this yields a burst pressure of approximately 514 N/m² — equivalent to a water column height of 5.2 cm. This value substantially exceeds the hydrostatic driving pressures generated by the fluid volumes employed in typical LFA operation, thereby effectively pinning the fluid within the drain pad and preventing reverse transport under normal assay conditions.

3. Device testing and Characterization:

3.1 Single diode characterization: Figure 2 (a-c) shows representative images of the forward flow progression through a single fluidic diode upon application of 1X PBS buffer solution containing 1% v/v Pluronic F127 surfactant to the source pad. Fig 2 (a-c) specifically shows the side-view images of fluid progression of the applied fluid over the source pad as it transitions from the source pad into the airgap region of the diode. As may be observed, fluid first saturates the source pad and thereby seamlessly entering the top and bottom thin capillary gaps formed about

the source pad. The capillary forces acting on the fluid front along with the hydrostatic pressure rapidly advances the fluid front across the air gap region of the diode delivering the fluid to the drain pad. The time taken for the fluid front to traverse the gap was observed to be within 2.7 ± 0.9 seconds (n = 10) for 1X PBS buffer with no surfactant in devices where the top and bottom bridging materials were plasma treated mylar (T&B PT Mylar). It should be noted that the dual-surface DST offset configuration employed on both faces of the source pad, as described in Section 2.2, ensures that the fluid front is guided between both the top and bottom Mylar surfaces upon entering the gap. This geometry therefore ensures seamless transition of fluid flow from a capillary driven flow within the porous glass fiber membrane to surface directed flow within the airgap, without the requirement for physical sidewalls to contain the flow within the airgap. This flow behavior thereby establishes the forward flow criteria for the fluidic diode where the impedance to the flow is minimal in this direction. A comprehensive summary of forward flow timing across all buffer conditions and device constructions tested is presented in Table 1.

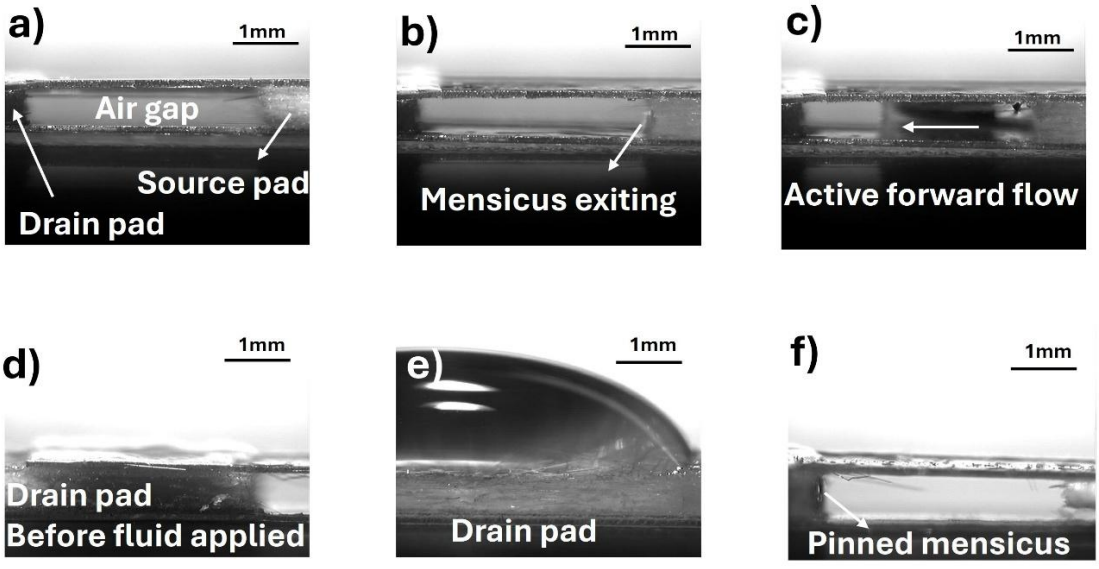


Figure 2: a)-c) Sideview photographs of the fluidic diode showing the progression of fluid (1X PBS solution, 1% Pluronic F127) through the airgap region in the forward flow regime, d)-f) shows the drain side fluid retention due to the stop valve geometry, (see supplementary information for the realtime video)

Figure 2 d)-f) shows the corresponding results for reverse flow retention. Upon application of an identical volume of buffer solution directly to the drain pad, no fluid breakthrough into the air gap was observed in any of the tested devices over the entire 5 minute observation period (n = 10). Fig. 2e shows representative images that shows the height of the liquid droplet over the drain pad (~ 5 mm). Fig. 2f shows the section of the saturated drain pad within the airgap. Despite the pad saturation and the excess hydrostatic pressure of the fluid within the pad by the applied droplet, there was no discernable meniscus appearing near the source pad termination within the airgap showing that the fluid was effectively pinned by the stop valve geometry. This observation was consistent with the burst pressure analysis presented in Section 2.3.

3.2 Compatibility with Lateral Flow Assay Fabrication

It is worth noting that the surface-directed flow architecture of the fluidic diode confers a significant practical advantage through its inherent compatibility with the established high-throughput fabrication processes employed in the manufacture of conventional lateral flow assays. In a conventional LFA, individual device components, the conjugate pad, nitrocellulose membrane, absorbent pad, and backing card, are assembled as a laminated stack and subsequently cut into individual test strips through a simple cutting operation. The fluidic diode modules described herein may be fabricated and assembled in an entirely analogous manner. Because lateral confinement of the fluid within the air gap is achieved through surface-directed flow rather than through physically defined channel walls, there is no requirement for precision microfabrication or enclosed channel structures. The constituent layers which include the source and drain paper pads, the bridging Mylar sheet, and the DST layers, may be assembled as a planar laminated stack over large area sheets and laminated directly together with the LFA components during the standard assembly process. The resulting laminated assembly may then be cut into individual modular diode units through the same cutting operation used to singulate conventional LFA strips without any modification to the existing manufacturing

workflow. To that end, the fluidic diode architecture presented herein represents a manufacturable and scalable solution that may be seamlessly adopted within the existing lateral flow diagnostic manufacturing ecosystem.

3.3 Effect of Surfactant Concentration on Forward Flow and Reverse Flow Retention

Since the fluidic diodes primarily leverage the high surface tension of aqueous solutions to form the stop valves at the drain end (preventing reverse flows), any changes to the surface tension, particularly through additives that tend to lower the surface tension of the solutions can have a detrimental effect on the operation of the fluidic diode. To evaluate this and to ensure the applicability of fluidic diodes for real-world assay conditions where reagents such as running buffers and wash buffers often contain small quantities of added surfactants, we investigated the forward flow timing and reverse flow retention characteristics of the single diode under varying buffer conditions. Typical surfactant concentrations are relatively low - ten times below critical micellar concentrations of the surfactant employed, translating to (0.5 – 1% w/v) in actual assay conditions to prevent denaturing of captured proteins or dislodging specifically bound molecules at the test lines[26].

For these experiments, we chose Pluronic F127 as our surfactant and tested our devices at two different surfactant concentrations (0.5% and 1% v/v). Side view images of the fluidic diode after the application of the buffer solution (See fig. 2f) did not show discernable difference in the fluid meniscus at the drain side at both the surfactant concentrations compared to the buffer only solution indicating that the stop valve at the drain side did not get compromised at these concentrations of surfactant thereby preserving the fluidic diode unidirectional flow behavior. Further, across all buffer conditions tested (PBS, 0.5% and 1% Pluronic F127 v/v), no bursting of the stop valve was observed for the entire duration of drain stress testing, irrespective of the surfactant concentration employed. This result demonstrates that the stop valve geometry

remains robust against the hydrostatic pressures applied during testing even in the presence of surfactant additives at these concentrations for extended time durations.

Table 1 provides a summary of forward flow timing for single fluidic diode devices across buffer conditions and device constructions. For these studies, two device constructions were investigated: 1) single fluidic diodes constructed such that the bridging top and bottom substrates were both plasma treated Mylar films (T&B PT Mylar devices) 2) Single fluidic diodes such that only the top bridging film was plasma treated Mylar whereas the bottom substrate was standard LFA backing card with adhesive exposed (PT Mylar + Backing Card devices). “Time to exit inlet pad” is the elapsed time from initial fluid application to fluid exiting the inlet pad (saturation + exit intervals combined). “Time to cross airgap” is the elapsed time from pad exit to first contact with the drain pad. T&B PT Mylar devices: n = 10; PT Mylar + Backing Card devices: n = 5. The backing card substrate is significantly more hydrophobic than plasma-treated Mylar, which accounts for the substantially longer and more variable flow times observed in that construction.

Table 1: Summary of forward flow timing for single fluidic diode devices across buffer conditions and device constructions.

Buffer	Device Construction	Time to Exit Inlet Pad (s)	Time to Cross Airgap (s)
PBS	T&B PT Mylar	8.9 ± 8.1	2.7 ± 0.9
0.5% Pluronic F127	T&B PT Mylar	3.5 ± 1.4	3.1 ± 1.0
1% Pluronic F127	T&B PT Mylar	3.7 ± 1.4	3.2 ± 1.5
PBS	PT Mylar + Backing Card	47.2 ± 31.1	66.6 ± 40.9
0.5% Pluronic F127	PT Mylar + Backing Card	8.6 ± 2.1	6.8 ± 1.1
1% Pluronic F127	PT Mylar + Backing Card	11.0 ± 4.5	9.6 ± 2.7

As may be observed from Table 1, the addition of Pluronic F127 at 0.5% v/v resulted in markedly faster pad exit times compared to PBS alone (3.5 ± 1.4 s versus 8.9 ± 8.1 s for T&B PT Mylar, n = 10), with no further significant change at 1% v/v (3.7 ± 1.4 s). Airgap crossing times were comparable across all three buffer conditions (2.7–3.2 s for T&B PT Mylar), indicating that the surfactant primarily accelerated pad wetting and exit rather than altering flow behavior within the airgap itself across the top and bottom Mylar surfaces. The reduction in pad exit time with Pluronic F127 is consistent with improved wettability of the glass fiber membrane at these surfactant concentrations.

In the case of devices constructed wherein the bottom substrate was formed of an LFA backing card with adhesive exposed, similar trends for the pad exit times, although absolute times were substantially longer owing to the hydrophobic nature of the backing card substrate (table 1).

Notably, airgap transit time was dramatically slower for PBS in the backing card construction which is attributed to the hydrophobic exposed adhesive of the backing card forming the bottom airgap surface. Addition of Pluronic F127 substantially improved the timing — airgap crossing improved ~9.8-fold at 0.5% (6.8 ± 1.1 s) and ~6.9-fold at 1% (9.6 ± 2.7 s) relative to PBS, with a concurrent reduction in variability (CV from ~61% to ~16%), consistent with the surfactant partially wetting the hydrophobic backing card surface and improving fluid flow. These results indicate that for backing card constructions, inclusion of an appropriate surfactant in the running buffer is particularly important for achieving reliable and consistent forward flow.

3.4 Cascaded Diode Flow Sequencing

Figure 3a shows as schematic illustration of a cascaded fluidic diode construction consisting of 3 fluidic diode stages. In this configuration, the drain pad of each upstream diode unit serves simultaneously as the source pad of the immediately downstream diode unit, such that a single paper pad is shared between adjacent diode stages. As may be observed from Figure 3b, fluid applied to each source pad progressed unidirectionally through its corresponding air gap and into the downstream drain pad in a sequential manner, with no evidence of reverse flow from any drain pad into its upstream air gap at any point during the experiment (see supplementary information: Video).

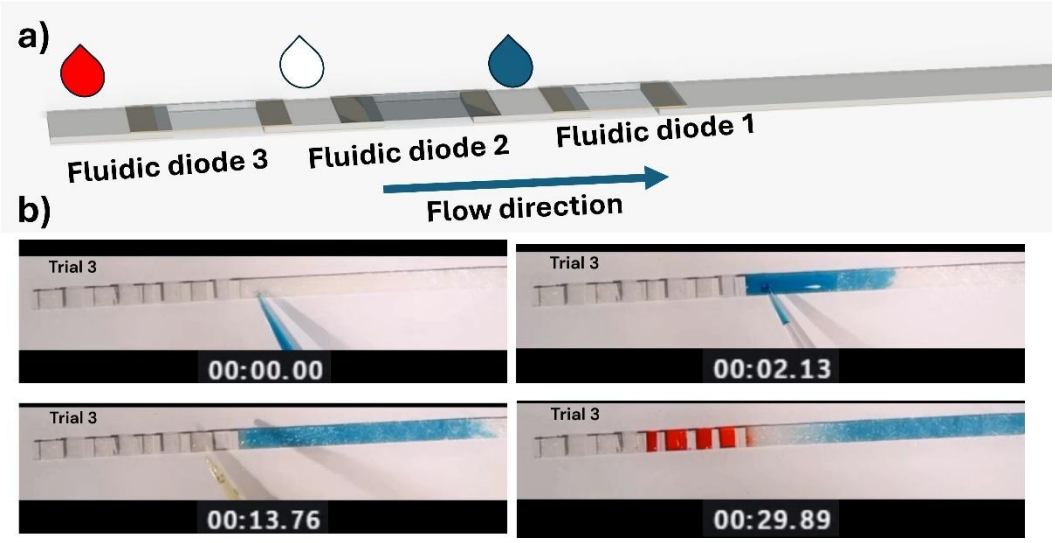


Figure 3 a) Schematic illustration of the cascaded fluidic diode construction, b) representative images from video recording at different time points (in seconds) showing the progression of different colored fluids through the series of the cascaded fluidic diodes.

It is important to note that mixing between adjacent fluid zones during the sequential delivery process is expected to be minimal, provided that forward flow occurs with sufficiently low resistance through each diode stage. This is consistent with the established behavior of laminar flows in paper-based microfluidic systems, where fluids occupying adjacent zones within porous media have been shown to mix predominantly through diffusion in the absence of convective driving forces [27]. The observed sharpness of the color boundaries between adjacent dye zones in Figure3b further supports observation.

It should be noted, however, that this favorable condition fails as the number of cascaded stages increases beyond a certain number. Capillary-driven flow in porous media follows Washburn dynamics, wherein the advancing fluid velocity decreases as $v \sim t^{-1/2}$ owing to the progressively increasing viscous resistance of the fluid-filled pore network[28]. In a cascaded assembly, increasing fluidic resistance progressively reduces the downstream fluid velocity such that, beyond a critical number of stages, the upstream fluid front may arrive at the downstream fluid which is advancing slowly, resulting in convective intermingling of the two fluid zones rather than

sharp plug-like displacement. This consideration places a practical upper limit on the number of diode stages that may be cascaded while preserving well-defined sequential reagent delivery.

3.5 Performance of the Fluidic Diode-Integrated SARS-CoV-2 LFA

The overall device architecture for the SARS-CoV-2 fluidic diode-integrated LFA is illustrated schematically in Figure 4a. The complete assembly was constructed on a single plastic backing card and comprised, in order from upstream to downstream: a (chase) buffer pad, an Au nanoparticle-loaded gold conjugate pad, a single fluidic diode region consisting of a 2 mm air gap and a 4 mm transfer pad, a nitrocellulose membrane bearing the test and control lines, and a terminal absorbent pad. This single-diode architecture located at the nitrocellulose entrance enforces a sample-first flow sequence. Sample applied directly to the transfer pad immediately enters the nitrocellulose without backflow. Subsequent application of the chase buffer applied to the buffer pad reconstitutes the gold conjugate and the resulting conjugate-laden buffer is subsequently driven across the diode and into the nitrocellulose detection zone. Figure 4b shows a representative photograph of the physical embodiment. Figure 4c shows the completed test results for the fluidic diode-integrated SARS-CoV-2 LFA alongside the conventional LFA control at matched antigen concentrations ranging down to 1 ng/mL of SARS-CoV-2 recombinant protein for the tests performed on two distinct days on different sets of devices. The fluidic diode-integrated LFA facilitated decoupling of the sample and conjugate flows through it, thereby transforming the device into a diagnostic strip capable of performing a two-step binding assay. As may be observed from Figure 4c, both devices produced clearly visible test and control lines across the concentration range tested. Fig 4d shows a close-up view of the obtained test results for the 1ng/ml concentration tested. It is evident that the two stage LFA produced a distinct non-uniformly developed signal compared to the more homogenous signal development for the conventional LFA. Specifically, the signal was more concentrated on the upstream edge of the detection region. This spatial inhomogeneity of the test line signal is consistent with the behavior

reported by Liang et al. for sequential reagent delivery in a sandwich immunoassay, wherein decoupling the introduction of sample and conjugate in time was shown to produce a binding profile sharply localized to the upstream edge of the detection region[29]. This arises from preferential capture of free analyte at the leading edge of the capture antibody zone prior to conjugate arrival. Further, densitometric analysis of the test line gray value profiles (See supplementary information) revealed that the fluidic diode-integrated device produced a test line intensity approximately 2.5 times greater than that of the conventional single-flow LFA control at matched antigen concentration. The gray-scale profile also depicted a steeper curve for the two stage LFA test line compared to the conventional LFA, consistent with our visual observation.

The 2.5-fold enhancement we observed was consistent with the general trend in signal intensities comparing the two reagent delivery formats reported by Liang et. al[29]. Liang et al. demonstrated that sequential delivery (two stage LFA) can yield a 4 to 10-fold improvement in the limit of detection relative to the conventional premix format depending on conjugate concentration. This suggests that further enhancement in signal intensity is possible through further optimization in binding constants of the antibody-antigen binding pairs and capture and conjugate concentration to be used for the assay. A full optimization and a limit of detection study for the two stage LFA would be the subject of a future publication. Our primary goal in this paper was to demonstrate that incorporation of the fluidic diode modules into the LFA architecture does not detrimentally affect signal generation, confirming fluidic diodes compatibility with standard LFA components and manufacturing methods.

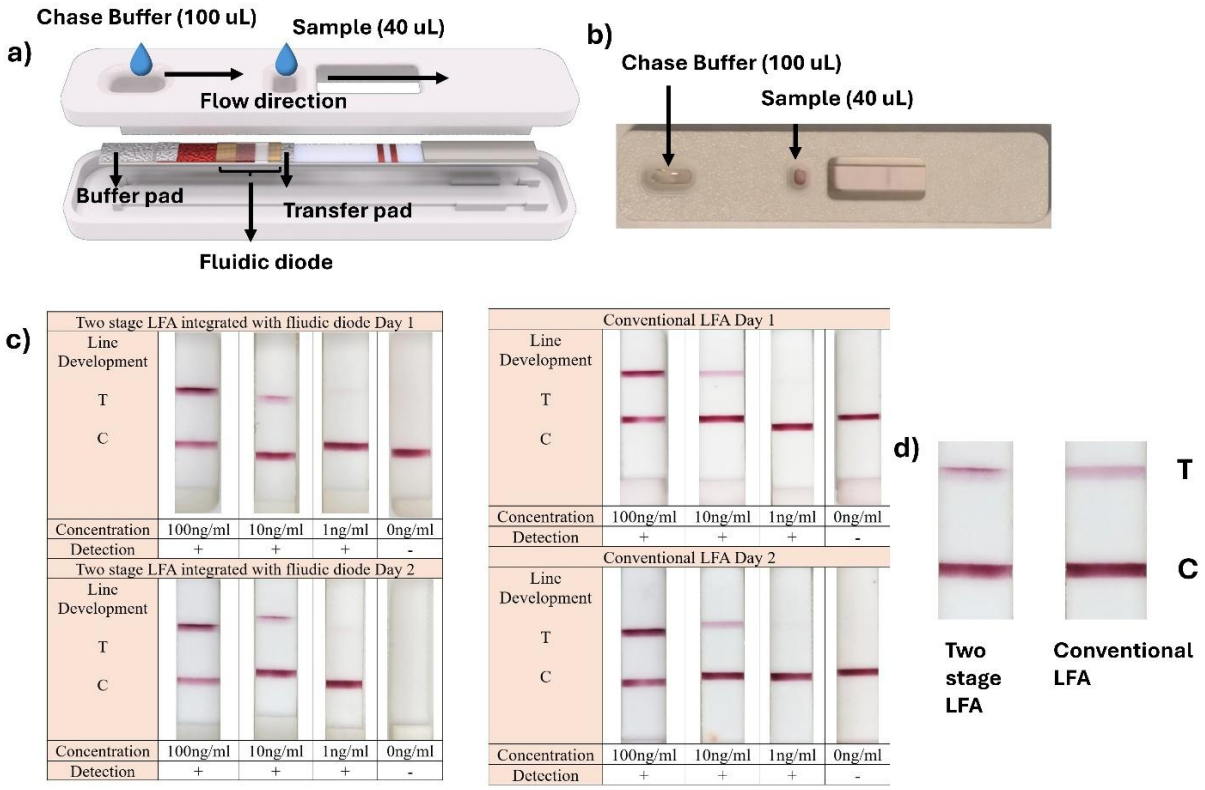


Figure 4. a) Schematic illustration of the two-stage SARS-CoV-2 fluidic diode-integrated LFA and b) Representative photograph of an actual two stage LFA device, c) completed test results for the two stage fluidic diode-integrated SARS-CoV-2 LFA alongside the conventional LFA control and d) close-up image of the test results (1ng/ml) comparing the two stage LFA to that of the conventional LFA.

The decoupling of sample and conjugate flows in a two-step binding assay has also been demonstrated in commercially available assays. Chembio Diagnostic Systems developed the Dual Path Platform (DPP®), wherein the sample and conjugate are delivered to the test line along independent, physically separated flow paths. This geometry has been reported to reduce interference between the immunoglobulins in the biological sample and their conjugate proteins while running a serological assay and has been shown to deliver improved sensitivity while minimizing the Hook effect [30], [31]. The fluidic diode architecture achieves the same functional decoupling of sample and conjugate flows as the DPP® platform, but in a fully inline, single-strip geometry that significantly reduces device footprint and fabrication complexity.

It should be noted that in the current implementation, the sample was first applied to the device and allowed to flow along the LFA strip, followed by the application of running buffer after a manually timed 5-minute interval. This timing interval was introduced to provide sufficient time for the sample to flow through the nitrocellulose membrane minimizing convective mixing between the reconstituted conjugate and the applied sample at the downstream detection zone. It is worth noting, however, that the air gap region separating the source and drain pads within each fluidic diode stage introduces new opportunities for controlling fluid transitions in a passive, time-delayed manner. For example, through modulation of the gap geometry, surface wettability, or the incorporation of hydrophobic delay features within the gap, it may be possible to realize well-defined, autonomous timing of the conjugate release step without user intervention. Leveraging these passive timing strategies to eliminate the manual incubation step and realize a fully autonomous two-step LFA will be the subject of future work.

4. Conclusions

In this paper, we have reported the design, fabrication, and characterization of hybrid paper–plastic fluidic diode modules and their seamless integration into a conventional lateral flow assay format for multi-step diagnostic assay applications. The fluidic diode enforces a unidirectional flow of the applied fluid from the source pad to the drain pad. The operating principle of the fluidic diode rests on the formation of a stop valve geometry on the drain side and a free flow geometry on the source side by the manner of placement of the bridging plastic sheet connecting the source and the drain pads. Single diode characterization confirmed reliable forward flow initiation and robust reverse flow prevention across all tested devices.

Systematic investigation of the effect of surfactant concentration on diode performance was conducted and the capillary stop valve function was observed to be preserved under buffer conditions typically used in an assay. Cascaded diode assemblies demonstrated well-defined sequential, unidirectional fluid delivery through multiple reagent stages, with dye visualization

experiments confirming that inter-zone mixing between adjacent fluid fronts is minimal and diffusion-limited in nature. Integration of the cascaded diode architecture into a two-step SARS-CoV-2 LFA successfully demonstrated a working two step binding assay in an inline format. It is worth noting that a particularly significant attribute of the fluidic diode architecture reported herein is its inherent compatibility with the established manufacturing processes of conventional lateral flow diagnostics. Because lateral fluid confinement within the air gap is achieved through surface-directed flow rather than through physically defined channel walls, the device components may be assembled as a planar laminated stack and singulated into individual test strips through the same cutting operations employed in conventional LFA strip manufacturing, without any requirement for precision microfabrication or specialized equipment. This fabrication compatibility, combined with the low material cost of the device components and the modularity of the cascaded diode design, positions the fluidic diode as a practically deployable solution for introducing multi-step reagent sequencing into lateral flow diagnostics while preserving the simplicity, low cost, and user-friendliness that are central to the platform's broad appeal in point-of-care and resource-limited settings.

5. Experimental:

Materials

Glass fiber conjugate pads (GFCP203000, SureWick G041, Millipore Sigma) were used for fabrication of the source and drain pads for all fluidic diode devices reported in this study. Hydrophilic Mylar polyester film (PP2500 Plain Paper Copier Transparency Film, 3M; thickness: ~200 μm) was used as the bridging sheet spanning the air gap between the source and drain pads. Hydrophobic double-sided adhesive tape (DST) (Scotch Brand, 3M; thickness: ~88.9 μm) was used for assembly of the fluidic diode on both the source and drain sides as described below.

Details on the monoclonal antibodies used for the production of the single stage and two stage LFA's may be obtained from ref [32]. All aqueous solutions were prepared using 1X PBS unless otherwise stated.

Fabrication of the Single Fluidic Diode

Figure 1 shows the schematic of the a single fluidic diode unit. Source and drain pads were cut from glass fiber membranes to dimensions of 16 mm × 4 mm using a precision cutting tool (thin-sheet paper cutter, manual guillotine-style cutter). The bridging Mylar sheet was cut to dimensions of ~330 mm × 102 mm, sized to span the full width of both paper pads as well as the air gap separating them.

Assembly of the fluidic diode proceeded as follows. A strip of DST of width ~3 mm was first applied to the underside of the Mylar sheet at the source-side edge. The DST was aligned such that it made contact with the top surface of the source pad while leaving a deliberate lateral offset of 3 mm between the DST edge and the leading edge of the source pad, thereby preserving a thin open capillary gap of height defined by the DST thickness (~88.9 μm) between the underside of the Mylar sheet and the top surface of the source pad. This offset is repeated on the underside of the conjugate pad source end. 13 mm of tape is placed on the underside of the conjugate pad such that the tape covers the region from 3 mm to 16 mm (i.e., 13/16 mm of the total pad length), leaving the first 3 mm fully uncovered; this uncovered region aligns directly with the 3 mm × ~88.9 μm capillary gap formed beneath the conjugate pad.

On the drain side, assembly of the capillary stop valve was achieved by applying DST strips of width ~3 mm (top) and ~12 mm (bottom) to both the top and bottom faces of the drain pad, with each strip aligned to remain flush with the leading edge of the drain pad. The air gap length between the trailing edge of the source pad and the leading edge of the drain pad was set to 4 mm for all devices reported in this study unless otherwise stated. All assembly steps were

performed on a flat, clean surface to ensure planarity of the laminated stack and consistency of the gap geometry across devices.

Fabrication of Cascaded Fluidic Diode Assemblies

For multi-reagent sequencing experiments, individual fluidic diode units were cascaded in series as illustrated in Figure 3a. In this configuration, the drain pad of each upstream diode unit serves simultaneously as the source pad of the immediately downstream diode unit, such that a single paper pad is shared between adjacent diode stages. The number of cascaded stages employed in this study was 4mm, yielding a total assembled length of 80 mm. Inter-stage air gap lengths and DST configurations were maintained identical to those described for the single diode unless otherwise stated.

Integration of Fluidic Diode Modules with Conventional Lateral Flow Assay Strips:

Un-assembled LFA components – including the conjugate pad and nitrocellulose striped with capture antibodies were produced at University of Nevada – Reno labs, the details of which may be obtained from [32].

Assembly of the fluidic diode integrated LFA device (Two stage LFA) proceeded as follows. The device assembly was made on a backing card 70mmX150mm . The nitrocellulose membrane 24mm × 4mm, ~100um thick) was first laminated onto the backing card using the adhesive backing of the membrane itself, positioned such that its proximal end was aligned with the intended conjugate pad interface zone. The absorbent pad (~18mm × 4mm, 0.5mm thick) was placed at the distal end of the nitrocellulose membrane with an overlap of 2 mm to ensure continuous wicking of fluid through the detection zone and into the absorbent reservoir.

Preparation of the Transfer pad (serving as the drain of the diode)

Immediately upstream of the nitrocellulose, a 4 mm × 4 mm transfer pad made from untreated conjugate pad material was placed. 2 mm of double-sided tape was applied to both the top and bottom faces of the transfer pad, aligned to the back end (toward the buffer pad), leaving 2 mm at the front end (toward the absorbent pad) with no tape. The 2 mm untaped front region was placed directly on top of the nitrocellulose membrane, forming the fluid-transfer interface. The transfer pad serves as the sample application zone, and the sample applied here immediately enters the nitrocellulose.

A 2 mm air gap was then established immediately upstream of the transfer pad. This gap begins at the back edge of the taped region of the transfer pad and extends 2 mm upstream, terminating at the floating edge of the gold conjugate pad.

The Au nanoparticle-loaded gold conjugate pad (20 mm × 4 mm) was positioned upstream of the 2 mm air gap. 17 mm of DST was applied to the bottom face of the conjugate pad, aligned to the back end of the pad, leaving 3 mm of untaped conjugate at the front end to form the floating edge. No DST was applied to the top face of the conjugate pad except for the 3 mm region where the bridging Mylar attaches. This configuration preserves the floating-edge behavior required for diode function.

The bridging Mylar sheet (10 mm × 4 mm) was then placed over the diode region. The front 3 mm of the Mylar contacted the DST on the top face of the transfer pad, the central 4 mm of the Mylar remained untaped and spanned the 2 mm air gap, and 3 mm of DST was manually added to the underside of the back end of the Mylar to secure it to the gold conjugate pad. When the Mylar was pressed down, the alignment of the 3 mm DST on the Mylar with the 17 mm DST on the underside of the gold conjugate pad created a 3 mm floating edge on the conjugate pad, with no tape above or below this region.

Buffer Pad Placement and Function

Upstream of the gold conjugate pad, a 12 mm × 4 mm buffer pad was placed, with 7 mm of the buffer pad overlapping the back end of the gold conjugate pad. The buffer pad was bonded to the backing card using 5 mm of DST applied to its bottom face, aligned to the back end of the pad, leaving 7 mm of untaped material at the front end to permit overlap onto the gold conjugate pad. No DST was applied to the top face of the buffer pad.

The buffer pad ensures that all reconstituted gold conjugate is driven forward across the diode. When buffer is applied directly to the gold conjugate pad without a buffer pad, the fluid spreads radially within the conjugate pad, causing a portion of the gold to remain behind rather than being pushed forward. By providing 7 mm of overlap and 4 mm of non-overlap space upstream, the buffer pad ensures that any radial spreading occurs within the buffer pad itself, while the full volume of reconstituted gold is directed forward toward the diode and into the nitrocellulose. Cut excess material if needed.

The completed laminated assembly was then loaded into the 3D printed cassette as described in supplementary information, with the buffer pad aligned beneath its corresponding fluid application port and stop feature.

Fabrication of the conventional lateral flow assay: For the fabrication of the conventional LFA, components were assembled as a large-format sheet on an adhesive backing card measuring 65mm in length along the flow direction. The assembled sheet comprised, in order from upstream to downstream: A blank glass fiber sample pad (10mm), a gold nanoparticle loaded conjugate pad (20mm as supplied by University of Nevada-Reno team), A nitrocellulose membrane (24 mm) bearing the test and control lines and an absorbent pad (20mm). The blank sample pad was positioned upstream of the gold conjugate pad, overlapping it by 5mm. The gold conjugate pad overlapped the upstream end of the nitrocellulose membrane by 2 mm. The absorbent pad overlapped the downstream end of the nitrocellulose membrane by 2 mm, with the remaining 18 mm of its length resting on the backing card. The exposed, non-overlapping 5 mm region of the

sample pad served as the single application port for both the sample and, following the wait period, the chase buffer. The completed laminated sheet was then cut into individual strips 4 mm in width using a precision cutting tool (thin-sheet paper cutter, manual guillotine-style cutter). Each fabricated strip was subsequently packaged into a custom 3D-printed cassette, fabricated in-house, to house the device during testing

Device Testing and Characterization

Single diode characterization: Forward flow through individual diode units was characterized by applying a fixed volume of 80 µL of buffer solution (PBS_and Pluronic F127_of different concentrations in PBS) to the source pad and recording the time elapsed from initial application to the appearance of fluid at the drain pad exit. A minimum of 10 devices were tested for each condition reported. Reverse flow retention was evaluated by applying an identical volume of buffer solution directly to the drain pad and recording whether fluid breakthrough into the air gap occurred within an observation period of 5 minutes. The effect of surfactant concentration on forward flow timing and reverse flow retention was investigated by preparing buffer solutions containing (Pluronic f127) at concentrations ranging from 0.5% to 1% % v/v in PBS. Imaging was performed using using a contact angle measurement unit (VCA Optima XE).

Cascaded diode flow visualization: Unidirectional flow through cascaded diode assemblies was visualized using aqueous dye solutions (Food coloring blue, red, yellow and or green in deionized water applied sequentially to the source pads of individual diode stages. Sequential image frames were captured at _20 second intervals to document the progression of fluid through the cascaded assembly.

Integrated LFA device testing: The performance of the fluidic diode-integrated LFA was evaluated using SARS-CoV-2 antigen samples prepared at concentrations ranging from 100ng/ml to 1 ng/ml in PBS containing 0.5% Pluronic. For each test, 40 µL of sample was applied to the transfer pad

of the cascaded diode assembly, followed by a 5 minute wait time. After this time is passed, 100 µL of chase buffer was applied to buffer pad in sequence.

For the tests performed on the conventional LFAs, the diluted viral sample was applied directly to the inlet reservoir opening to the sample pad in a volume of 40 µL, followed by a 5 minute wait time to allow the sample to flow through the device. After this time had passed, 90 µL of chase buffer was applied to the same application port to complete the run. Test line and control line intensities were recorded at 15 minutes post-sample running buffer application. A conventional single-flow LFA strip assembled with identical assay chemistries and nitrocellulose membrane was used as the control device for all comparative performance evaluations. Test strips were assembled at Northern Illinois University and shipped to University of Nevada-Reno and the tests were conducted on different devices on two different days. To evaluate the test results, ImageJ software was used to convert the captured image into a 32-bit grayscale image followed by measuring the grayscale values along across the test lines for both two stage device and the conventional device (see supplementary information).

Acknowledgements:

This work was supported by the Illinois Innovation Network, the Northern Illinois University Foundation, and the Northern Illinois University Research and Artistry Grant. The authors thank Dr. Sally McFall, Co-Director of the Center for Innovation in Global Health Technologies at Northwestern University, for helpful discussions and valuable suggestions throughout the course of this work.

References:

[1] B. G. Andryukov, “Six decades of lateral flow immunoassay: from determining metabolic markers to diagnosing COVID-19,” *AIMS Microbiol*, vol. 6, no. 3, pp. 280–304, Aug. 2020, doi: 10.3934/microbiol.2020018.

[2] “Lateral and Vertical Flow Assays for Point-of-Care Diagnostics - Jiang - 2019 - Advanced Healthcare Materials - Wiley Online Library.” Accessed: Aug. 15, 2022. [Online]. Available: https://onlinelibrary.wiley.com/doi/10.1002/adhm.201900244

[3] C. Carrell *et al.*, “Capillary driven microfluidic sequential flow device for point-of-need ELISA: COVID-19 serology testing,” *Anal. Methods*, vol. 15, no. 22, pp. 2721–2728, Jun. 2023, doi: 10.1039/D3AY00225J.

[4] A. O. Olanrewaju, A. Robillard, M. Dagher, and D. Juncker, “Autonomous microfluidic capillaric circuits replicated from 3D-printed molds,” *Lab on a Chip*, vol. 16, no. 19, pp. 3804–3814, 2016, doi: 10.1039/C6LC00764C.

[5] P. Novo, F. Volpetti, V. Chu, and J. P. Conde, “Control of sequential fluid delivery in a fully autonomous capillary microfluidic device,” *Lab on a chip*, vol. 13, Dec. 2012, doi: 10.1039/c2lc41083d.

[6] I. Jang, H. Kang, S. Song, D. S. Dandy, B. J. Geiss, and C. S. Henry, “Flow control in a laminate capillary-driven microfluidic device,” *Analyst*, vol. 146, no. 6, pp. 1932–1939, Mar. 2021, doi: 10.1039/D0AN02279A.

[7] Y. Arango, Y. Temiz, O. Gökçe, and E. Delamarche, “Electro-actuated valves and self-vented channels enable programmable flow control and monitoring in capillary-driven microfluidics,” *Science Advances*, vol. 6, no. 16, p. eaay8305, Apr. 2020, doi: 10.1126/sciadv.aay8305.

[8] V. A. Papadimitriou, L. I. Segerink, A. van den Berg, and J. C. T. Eijkel, “3D capillary stop valves for versatile patterning inside microfluidic chips,” *Analytica Chimica Acta*, vol. 1000, pp. 232–238, Feb. 2018, doi: 10.1016/j.aca.2017.11.055.

[9] V. G. Panferov, A. V. Zherdev, and B. B. Dzantiev, “Post-Assay Chemical Enhancement for Highly Sensitive Lateral Flow Immunoassays: A Critical Review,” *Biosensors (Basel)*, vol. 13, no. 9, p. 866, Sep. 2023, doi: 10.3390/bios13090866.

[10] M. O. Rodríguez, L. B. Covián, A. C. García, and M. C. Blanco-López, “Silver and gold enhancement methods for lateral flow immunoassays,” *Talanta*, vol. 148, pp. 272–278, Feb. 2016, doi: 10.1016/j.talanta.2015.10.068.

[11] W. Yang *et al.*, “A colloidal gold probe-based silver enhancement immunochromatographic assay for the rapid detection of abrin-a,” *Biosensors and Bioelectronics*, vol. 26, no. 8, pp. 3710–3713, Apr. 2011, doi: 10.1016/j.bios.2011.02.016.

[12] P. Nandhakumar *et al.*, “Redox Cycling Amplified Electrochemical Lateral-Flow Immunoassay: Toward Decentralized Sensitive Insulin Detection,” *ACS Sens.*, vol. 8, no. 10, pp. 3892–3901, Oct. 2023, doi: 10.1021/acssensors.3c01445.

[13] X. Ying *et al.*, “Electrochemical Lateral Flow Immunoassay with Built-In Electrodes for Ultrasensitive and Wireless Detection of Inflammatory Biomarkers,” *Anal. Chem.*, vol. 96, no. 26, pp. 10630–10638, Jul. 2024, doi: 10.1021/acs.analchem.4c01224.

[14] K. M. Clark *et al.*, “Electrochemical Capillary Driven Immunoassay for Detection of SARS-CoV-2,” *ACS Meas. Sci. Au*, vol. 2, no. 6, pp. 584–594, Dec. 2022, doi: 10.1021/acsmeasuresciau.2c00037.

[15] E. A. Phillips, R. Shen, S. Zhao, and J. C. Linnes, “Thermally actuated wax valves for paper-fluidic diagnostics,” *Lab Chip*, vol. 16, no. 21, pp. 4230–4236, Oct. 2016, doi: 10.1039/C6LC00945J.

[16] K. P. Jiang, S. Bennett, and P. Yager, “Heat-actuated valve implementation in a point-of-care, paper-based microfluidic device for infectious disease detection,” *PLoS One*, vol. 21, no. 4, p. e0344750, Apr. 2026, doi: 10.1371/journal.pone.0344750.

[17] D. Lee, T. Ozkaya-Ahmadov, C.-H. Chu, M. Boya, R. Liu, and A. F. Sarioglu, “Capillary flow control in lateral flow assays via delaminating timers,” *Science Advances*, vol. 7, no. 40, p. eabf9833, Oct. 2021, doi: 10.1126/sciadv.abf9833.

[18] B. J. Toley, B. McKenzie, T. Liang, J. R. Buser, P. Yager, and E. Fu, “Tunable-Delay Shunts for Paper Microfluidic Devices,” *Anal Chem*, vol. 85, no. 23, pp. 11545–11552, Dec. 2013, doi: 10.1021/ac4030939.

[19] X. Li, P. Zwanenburg, and X. Liu, “Magnetic timing valves for fluid control in paper-based microfluidics,” *Lab Chip*, vol. 13, no. 13, pp. 2609–2614, Jul. 2013, doi: 10.1039/c3lc00006k.

[20] H. Fu *et al.*, “A paper-based microfluidic platform with shape-memory-polymer-actuated fluid valves for automated multi-step immunoassays,” *Microsystems & Nanoengineering*, vol. 5, no. 1, Art. no. 1, Sep. 2019, doi: 10.1038/s41378-019-0091-0.

[21] Y. Patil *et al.*, “Modular design of paper based switches for autonomous lab-on paper micro devices,” *Biomed Microdevices*, vol. 23, no. 1, p. 1, Nov. 2020, doi: 10.1007/s10544-020-00537-w.

[22] B. J. Toley *et al.*, “A versatile valving toolkit for automating fluidic operations in paper microfluidic devices,” *Lab Chip*, vol. 15, no. 6, pp. 1432–1444, Mar. 2015, doi: 10.1039/C4LC01155D.

[23] T. Kong, S. Flanigan, M. Weinstein, U. Kalwa, C. Legner, and S. Pandey, “A fast, reconfigurable flow switch for paper microfluidics based on selective wetting of folded paper actuator strips,” *Lab Chip*, vol. 17, no. 21, pp. 3621–3633, Oct. 2017, doi: 10.1039/C7LC00620A.

[24] B. Zhao, J. S. Moore, and D. J. Beebe, “Surface-Directed Liquid Flow Inside Microchannels,” *Science*, vol. 291, no. 5506, pp. 1023–1026, Feb. 2001, doi: 10.1126/science.291.5506.1023.

[25] H. Cho, H.-Y. Kim, J. Y. Kang, and T. S. Kim, “How the capillary burst microvalve works,” *Journal of Colloid and Interface Science*, vol. 306, no. 2, pp. 379–385, Feb. 2007, doi: 10.1016/j.jcis.2006.10.077.

[26] L. J. Waters, J. Whiteley, W. Small, and S. Mellor, “Determining suitable surfactant concentration ranges to avoid protein unfolding in pharmaceutical formulations using UV analysis,” *Heliyon*, vol. 9, no. 11, p. e21712, Oct. 2023, doi: 10.1016/j.heliyon.2023.e21712.

[27] J. L. Osborn, B. Lutz, E. Fu, P. Kauffman, D. Y. Stevens, and P. Yager, “Microfluidics without pumps: reinventing the T-sensor and H-filter in paper networks†”, doi: 10.1039/c004821f.

[28] E. W. Washburn, “The Dynamics of Capillary Flow,” *Phys. Rev.*, vol. 17, no. 3, pp. 273–283, Mar. 1921, doi: 10.1103/PhysRev.17.273.

[29] T. Liang, R. Robinson, J. Houghtaling, G. Fridley, S. A. Ramsey, and E. Fu, “Investigation of Reagent Delivery Formats in a Multivalent Malaria Sandwich Immunoassay and

Implications for Assay Performance," *Anal. Chem.*, vol. 88, no. 4, pp. 2311–2320, Feb. 2016, doi: 10.1021/acs.analchem.5b04222.

[30] M. Gunasekera, M. Narine, M. Ashton, and J. Esfandiari, "Development of a Dual Path Platform (DPP®) immunoassay for rapid detection of *Candida albicans* in human whole blood and serum," *Journal of Immunological Methods*, vol. 424, pp. 7–13, Sep. 2015, doi: 10.1016/j.jim.2015.04.014.

[31] S. A. Nabity *et al.*, "Accuracy of a Dual Path Platform (DPP) Assay for the Rapid Point-of-Care Diagnosis of Human Leptospirosis," *PLOS Neglected Tropical Diseases*, vol. 6, no. 11, p. e1878, Nov. 2012, doi: 10.1371/journal.pntd.0001878.

[32] H. J. Hill *et al.*, "Comparison of a Prototype SARS-CoV-2 Lateral Flow IMMUNOASSAY with the BinaxNOWTM COVID-19 Antigen CARD," *Viruses*, vol. 14, no. 12, p. 2609, Nov. 2022, doi: 10.3390/v14122609.

Supplementary Files

This is a list of supplementary files associated with this preprint. Click to download.

- SUPPORTINGINFORMATION.docx
- CascadedFluidicDiodes.mp4
- ForwardFlowSingleDiode1PluronicF127.mp4
- StopValveatDrain1PluronicF127.mp4